Long-Term Rotational Motion Analysis and Comparison to Observations of the Inoperative Envisat

Luc B. M. Sagnières[*] and Inna Sharf[†]

McGill University, Montreal, Quebec H3A 0C3, Canada

A new model for the analysis and prediction of the rotational motion of large space debris over a long term is outlined. A formulation for a high-order gravity-gradient torque is derived as well as the aerodynamic torque for a spinning spacecraft defined by a general surface geometry model. The comprehensive model is exercised for a coupled orbit-attitude propagation of the defunct satellite Envisat. An in-depth analysis of the simulation results reveals that, unlike what has been assumed previously, the likelihood of Envisat's spin axis remaining stable is small. A distinct nutation of the spacecraft's angular momentum vector about the orbit normal is predicted, having a period on the order of a few days. Although a decay of the angular rate is expected, the nutation motion of the spin axis is expected to become larger and faster with time, underlining a potential difficulty for a future active debris removal mission. A critical review of observational studies reported on Envisat's rotational state is performed, in light of the knowledge gained from the simulations and with a comparison to the simulation results. Finally, recommendations for future observation campaigns to provide better estimates of Envisat's angular motion are put forward.

Nomenclature

A	=	surface area, m^2
$\boldsymbol{a}$	=	acceleration, m · s^{-2}
a	=	geomagnetic convention for Earth's mean reference spherical radius, m
a_u	=	astronomical unit, m
$\boldsymbol{B}$	=	magnetic field, T
C, S	=	spherical harmonic coefficients
$\boldsymbol{C}$	=	rotation matrix
c	=	speed of light, m · s^{-1}
c_D	=	drag coefficient
$\boldsymbol{c}_p$	=	position of center of pressure, m
g, h	=	Gauss coefficients
$\boldsymbol{h}$	=	angular momentum, kg · m^2 · s^{-1}
$\boldsymbol{I}$	=	inertia tensor, kg · m^2
$\boldsymbol{I}_d$	=	damper inertia tensor, kg · m^2
k_d	=	damping constant, kg · m^2 · s^{-1}
$\boldsymbol{M}$	=	magnetic tensor, kg^{-1} · m^2 · s^3 · A^2
m	=	spacecraft mass, kg
$\boldsymbol{n}$	=	surface normal
$\boldsymbol{n}_O$	=	orbit normal
$P_{l,m}$	=	Legendre functions
P_n^m	=	Schmidt normalized associated Legendre functions
$\boldsymbol{q}$	=	quaternion
$\boldsymbol{q}_d$	=	damper quaternion
R_E	=	Earth's equatorial radius, m
$\boldsymbol{r}$	=	position, m
$\boldsymbol{r}_1$	=	sun position, m
S_R	=	solar radiation constant, W · m^2
$\boldsymbol{s}$	=	incident light direction
t	=	time, s
U	=	gravitational potential, J · kg^{-1}
$\boldsymbol{v}$	=	velocity, m · s^{-1}
X, Y, Z	=	inertial frame axes
x, y, z	=	body-frame axes
x_h, y_h, z_h	=	angular momentum frame axes
x_O, y_O, z_O	=	orbital frame axes
x_P, y_P, z_P	=	precessing frame axes
α	=	angle between surface normal and incident flow, rad
β	=	angle between surface normal and incident light, rad
θ	=	latitude, rad
λ	=	longitude, rad
μ	=	standard gravitational parameters, m^3 · s^{-2}
ρ	=	atmospheric density, kg · m^{-3}
σ_a	=	absorption coefficient
σ_{rd}	=	diffuse reflection coefficient
σ_{rs}	=	specular reflection coefficient
$\boldsymbol{\tau}$	=	torque, m · N
ϕ	=	colatitude, rad
ϕ_s	=	solar radiation photon flux, W · m^{-2}
ψ	=	Earth shadow function
$\boldsymbol{\omega}$	=	angular velocity, rad · s^{-1}
$\boldsymbol{\omega}_d$	=	damper angular velocity, rad · s^{-1}

I. Introduction

RECENT years have seen a significant and growing interest in the modeling and observation of large space debris, motivated in part by space situational awareness but also with the view to ultimately removing these debris objects from orbit. In particular, the defunct European environmental satellite Envisat has been widely studied as a primary target for active debris removal (ADR), which involves capturing and deorbiting dangerous inoperative spacecraft from densely populated orbits [1]. The European Space Agency (ESA) is currently planning to launch its e.Deorbit mission, the world's first ADR mission, in 2023 with the goal of removing Envisat [2]. Understanding the rotational dynamics of the target, however, is fundamental for the success of such a mission. Although active spacecraft are either passively attitude-stabilized or have an attitude control system to compensate for small perturbations in their attitude, for tumbling debris in uncontrolled attitude states, even minute environmental effects can accumulate over time and cause a large unpredictable rotational motion, the dynamics of which are only now starting to be studied [3].

The European Space Agency lost contact with Envisat in April 2012, and a number of observatories around the world have since tracked the spacecraft to determine its rotational state. Three different methods have been used in the observation campaigns to date, including satellite laser ranging (SLR), photometric measurements

*Ph.D. Candidate, Department of Mechanical Engineering, 817 Sherbrooke Street West; luc.sagnieres@mail.mcgill.ca. Student Member AIAA.

†Professor, Department of Mechanical Engineering, 817 Sherbrooke Street West; inna.sharf@mcgill.ca. Associate Fellow AIAA.

(light curves), and inverse synthetic aperture radar (ISAR) images [4–6]. These observations have revealed that Envisat experienced a significant angular velocity increase through May 2013, unexplained thus far, and that since then the spacecraft has been undergoing a slow decay of its spin rate. Initial modeling efforts determined that this was due to the eddy-current torque as the spacecraft interacted with Earth's magnetic field [7]. Furthermore, ESA has contracted the development of a coupled orbit-attitude model for large space debris called ιOTA (In-Orbit Tumbling Analysis). Preliminary results with this model, which is still under development and not open to the public, have been published, focusing on reproducing synthetic measurements such as light curves and SLR residuals to compare to observations [8]. Although the observation studies published to date mostly agree on the satellite's spin rate, there are contradictions about the observed or determined motion of its spin axis and these are truly puzzling.

In this study, we make use of a newly developed coupled orbit-attitude propagation model, the most comprehensive thus far presented in the open literature, to predict the rotational dynamics of the "most wanted" space debris Envisat, over a four-year duration beginning after its spin-up in May 2013. A detailed gravity-gradient torque making use of high-order geopotential coefficients is derived. The expansion of the terms for the aerodynamic drag and torque for a spinning spacecraft as a function of a user-specified spacecraft surface geometry is given. The model will be presented, and new insights into the evolution of the satellite's angular motion will be detailed. Through analysis of the simulation results, we achieve our principal goal, which is to gain insight and new understanding of the attitude evolution of large space debris objects over a long period of time. With careful postprocessing of attitude time histories of Envisat, we identify three distinct components of the rotational motion of this debris, the understanding of which we hope will provide the community with new perspectives for further studies of Envisat's rotation. An in-depth review of previous observational studies dealing with Envisat's rotational motion is performed, taking into consideration the new knowledge gained from the simulation results. Finally, recommendations for future observation campaigns studying Envisat will be provided to gain a more complete understanding of its angular motion.

II. Coupled Orbit-Attitude Propagation Model

A. Model Description

Dealing with satellite dynamics requires an analysis of the six-degree-of-freedom governing the orbit and attitude of spacecraft. Three vector differential equations describe the evolution of the corresponding variables. First is the dynamics equation for orbital motion in an Earth-centered inertial coordinate frame [9]:

$$\ddot{\boldsymbol{r}}(t) = -\frac{\mu}{r(t)^3}\boldsymbol{r}(t) + \sum_j \boldsymbol{a}_j(t, \boldsymbol{r}(t), \boldsymbol{v}(t), \boldsymbol{q}(t), \boldsymbol{\omega}(t)) \quad (1)$$

where $\boldsymbol{r}$ is the position as a function of time t; $r = \|\boldsymbol{r}\|$; $\boldsymbol{v}$ is the velocity; $\boldsymbol{q}$ is the attitude parameterization, chosen here to be a quaternion, $\boldsymbol{q} = [q_0 \quad \boldsymbol{q}_v^T]^T$; $\boldsymbol{\omega}$ is the angular velocity of the body with respect to the inertial frame; $\mu = 3,986,004.418 \times 10^8 \text{ m}^3 \cdot \text{s}^{-1}$ is the Earth's gravitational parameter; and $\boldsymbol{a}_j$ represents the additional considered accelerations due to orbital perturbations. The specific inertial frame chosen is the true equator mean equinox frame of the initial chosen two-line element (TLE) epoch [10].

The second differential equation, the dynamics equation for attitude motion, relates the evolution of absolute angular velocity to the sum of the external torques $\boldsymbol{\tau}_j$ about the body's center of mass [11]:

$$\boldsymbol{I}\dot{\boldsymbol{\omega}}(t) + \boldsymbol{\omega}(t)^\times \boldsymbol{I}\boldsymbol{\omega}(t) = \sum_j \boldsymbol{\tau}_j(t, \boldsymbol{r}(t), \boldsymbol{v}(t), \boldsymbol{q}(t), \boldsymbol{\omega}(t)) \quad (2)$$

where $\boldsymbol{I}$ is the matrix representation of the inertia tensor of the rigid body in the centroidal body-fixed frame. All vectors in Eq. (2) represent components in the same body-fixed frame; the superscript × denotes the skew-symmetric matrix representation of the cross-product.

Table 1   External perturbations considered in the coupled orbit-attitude propagation model

Perturbation	Environmental model
Gravitational perturbations and gravity gradient torque	EGM2008 [13]
Third-body perturbations	Astronomical Almanac [9]
Aerodynamic drag and torque	DTM-2013 [15]; HWM14 [16]
Eddy-current torque	IGRF-12 [18]
Solar radiation pressure and torque	Montenbruck and Gill [19]
Internal energy dissipation	Kane damper [20]
Hypervelocity impacts	MASTER-2009 [21]

Finally, the third differential equation is the kinematic equation for the absolute orientation of the spacecraft:

$$\dot{\boldsymbol{q}}(t) = \frac{1}{2}\boldsymbol{\Omega}(\omega)\boldsymbol{q}(t) \quad (3)$$

where, expressed in terms of the body-frame components of $\boldsymbol{\omega}$,

$$\boldsymbol{\Omega} = \begin{bmatrix} 0 & -\omega_x & -\omega_y & -\omega_z \\ \omega_x & 0 & \omega_z & -\omega_y \\ \omega_y & -\omega_z & 0 & \omega_x \\ \omega_z & \omega_y & -\omega_x & 0 \end{bmatrix} \quad (4)$$

In the present work, Eqs. (1–3) are numerically propagated using a fifth-order Runge–Kutta method called the Runge–Kutta Dormand–Prince numerical integration method [12].

The accelerations and torques due to external perturbations, as well as the environmental models considered, are summarized in Table 1 and defined in detail in the following paragraphs. These include Earth's gravitational acceleration due to its deviation from that of a homogeneous sphere, the gravity-gradient torque, and third-body gravitational accelerations from the sun and the moon, all of which are conservative, as well as the aerodynamic drag and torque, the eddy-current torque, and the solar radiation pressure and torque, which are dissipative. An emphasis on the gravity-gradient torque and the aerodynamic torque is made as a more complete form than typically used is derived. The effect of hypervelocity impacts and internal energy dissipation are also discussed.

1. Gravitational Perturbations

To derive the acceleration due to Earth gravitational perturbations, the spherical-harmonic expansion of the gravitational potential function U defining the Earth's gravitational field as a function of a satellite's distance to Earth's center (r), its spherical geocentric latitude θ, and its longitude λ, can be used [9]:

$$U(r, \theta, \lambda) = \frac{\mu}{r}\left[1 + \sum_{l=2}^{k}\sum_{m=0}^{l}\left(\frac{R_E}{r}\right)^l P_{l,m}[\sin\theta]\{C_{l,m}\cos(m\lambda) + S_{l,m}\sin(m\lambda)\}\right] \quad (5)$$

where $R_E = 6378.1363$ km is Earth's equatorial radius, C and S are coefficients representing the mathematical modeling for the Earth's shape using spherical harmonics, and $P_{l,m}$ are Legendre functions evaluated at $\sin\theta$. The sum is performed over the gravitational coefficients as obtained from the Earth Gravitational Model 2008 (EGM2008) up to degree and order $k = 12$ [13]. The acceleration due to Earth's gravitational field is computed using the chain rule as:

$$\boldsymbol{a}_{\text{grav}} = \frac{\partial U}{\partial r}\left(\frac{\partial r}{\partial \boldsymbol{r}}\right)^T + \frac{\partial U}{\partial \lambda}\left(\frac{\partial \lambda}{\partial \boldsymbol{r}}\right)^T + \frac{\partial U}{\partial \theta}\left(\frac{\partial \theta}{\partial \boldsymbol{r}}\right)^T \quad (6)$$

The gravity-gradient torque is usually calculated assuming a spherical model of Earth's gravity field. However, it can also be

computed in the body frame for a general gravitational field. Assuming that gravity in the vicinity of the center of mass varies linearly, the gravity-gradient torque is given as follows [14]:

$$
\boldsymbol{\tau}_{\text{grav}} = \begin{bmatrix} g_{23}(I_{zz} - I_{yy}) - g_{13}I_{xy} + g_{12}I_{xz} + I_{yz}(g_{22} - g_{33}) \\ g_{13}(I_{xx} - I_{zz}) + g_{23}I_{xy} - g_{12}I_{yz} + I_{xz}(g_{33} - g_{11}) \\ g_{12}(I_{yy} - I_{xx}) - g_{23}I_{xz} + g_{13}I_{yz} + I_{xy}(g_{11} - g_{22}) \end{bmatrix} \quad (7)
$$

where the g_{ij} and I_{ij} are the components of the matrices $\boldsymbol{G}$ and $\boldsymbol{I}$, respectively, with the former defined by

$$
\boldsymbol{G} = \boldsymbol{C}^T \frac{\partial \boldsymbol{a}_{\text{grav}}}{\partial \boldsymbol{r}} \boldsymbol{C} \quad (8)
$$

and where $\boldsymbol{C}$ is the rotation matrix from the body-fixed frame to the inertial frame.

The evaluation of $\boldsymbol{G}$ requires the derivative of $\boldsymbol{a}_{\text{grav}}$ with respect to $\boldsymbol{r}$, which can be computed analytically. Thus, using the aspherical-potential function of Eq. (5) directly, the derivative of the acceleration can be computed from Eq. (6) by again applying the chain rule:

$$
\frac{\partial \boldsymbol{a}_{\text{grav}}}{\partial \boldsymbol{r}} = \frac{\partial^2 U}{\partial r^2} \frac{\partial r}{\partial \boldsymbol{r}} \left(\frac{\partial r}{\partial \boldsymbol{r}}\right)^T + \frac{\partial^2 U}{\partial \theta^2} \frac{\partial \theta}{\partial \boldsymbol{r}} \left(\frac{\partial \theta}{\partial \boldsymbol{r}}\right)^T + \frac{\partial^2 U}{\partial \lambda^2} \frac{\partial \lambda}{\partial \boldsymbol{r}} \left(\frac{\partial \lambda}{\partial \boldsymbol{r}}\right)^T
$$
$$
+ \frac{\partial^2 U}{\partial \theta \partial r} \left(\frac{\partial r \partial \theta^T}{\partial \boldsymbol{r} \partial \boldsymbol{r}} + \frac{\partial \theta \partial r^T}{\partial \boldsymbol{r} \partial \boldsymbol{r}}\right) + \frac{\partial^2 U}{\partial \lambda \partial r} \left(\frac{\partial r \partial \lambda^T}{\partial \boldsymbol{r} \partial \boldsymbol{r}} + \frac{\partial \lambda \partial r^T}{\partial \boldsymbol{r} \partial \boldsymbol{r}}\right)
$$
$$
+ \frac{\partial^2 U}{\partial \theta \partial \lambda} \left(\frac{\partial \lambda \partial \theta^T}{\partial \boldsymbol{r} \partial \boldsymbol{r}} + \frac{\partial \theta \partial \lambda^T}{\partial \boldsymbol{r} \partial \boldsymbol{r}}\right) + \frac{\partial U}{\partial r} \frac{\partial^2 r}{\partial \boldsymbol{r}^2} + \frac{\partial U}{\partial \theta} \frac{\partial^2 \theta}{\partial \boldsymbol{r}^2} + \frac{\partial U}{\partial \lambda} \frac{\partial^2 \lambda}{\partial \boldsymbol{r}^2} \quad (9)
$$

The second partial derivatives of the aspherical-potential function are calculated as follows:

$$
\frac{\partial^2 U}{\partial r^2} = \frac{\mu}{r^3} \left[2 + \sum_{l=2}^{k} \sum_{m=0}^{l} \left(\frac{R_E}{r}\right)^l (l+1)(l+2) P_{l,m} \{C_{l,m} \cos(m\lambda) \right.
$$
$$
\left. + S_{l,m} \sin(m\lambda)\} \right] \quad (10)
$$

$$
\frac{\partial^2 U}{\partial \theta^2} = \frac{\mu}{r} \sum_{l=2}^{k} \sum_{m=0}^{l} \left(\frac{R_E}{r}\right)^l \{P_{l,m+2} - (2m+1)\tan(\theta)P_{l,m+1}
$$
$$
+ m(m\tan(\theta) - \sec^2(\theta))P_{l,m}\} \times \{C_{l,m}\cos(m\lambda) + S_{l,m}\sin(m\lambda)\} \quad (11)
$$

$$
\frac{\partial^2 U}{\partial \lambda^2} = \frac{\mu}{r} \sum_{l=2}^{k} \sum_{m=0}^{l} \left(\frac{R_E}{r}\right)^l m^2 P_{l,m} \{-S_{l,m}\sin(m\lambda) - C_{l,m}\cos(m\lambda)\} \quad (12)
$$

$$
\frac{\partial^2 U}{\partial \theta \partial r} = -\frac{\mu}{r^2} \sum_{l=2}^{k} \sum_{m=0}^{l} \left(\frac{R_E}{r}\right)^l (l+1)\{P_{l,m+1} - m\tan(\theta)P_{l,m}\}
$$
$$
\times \{C_{l,m}\cos(m\lambda) + S_{l,m}\sin(m\lambda)\} \quad (13)
$$

$$
\frac{\partial^2 U}{\partial \lambda \partial r} = -\frac{\mu}{r^2} \sum_{l=2}^{k} \sum_{m=0}^{l} \left(\frac{R_E}{r}\right)^l m(l+1)P_{l,m} \{S_{l,m}\cos(m\lambda)
$$
$$
- C_{l,m}\sin(m\lambda)\} \quad (14)
$$

$$
\frac{\partial^2 U}{\partial \theta \partial \lambda} = \frac{\mu}{r} \sum_{l=2}^{k} \sum_{m=0}^{l} \left(\frac{R_E}{r}\right)^l m\{P_{l,m+1} - m\tan(\theta)P_{l,m}\} \times \{S_{l,m}\cos(m\lambda)
$$
$$
- C_{l,m}\sin(m\lambda)\} \quad (15)
$$

Furthermore, the coordinate transformations, $\partial^2 r/\partial \boldsymbol{r}^2$, $\partial^2 \theta/\partial \boldsymbol{r}^2$, etc., can all be derived in closed form and are presented in Appendix A.

The final gravitational perturbation considered is third-body accelerations. They are determined from μ_k and $\boldsymbol{r}_k$ representing the gravitational parameter and position of the sun and moon ($k = 1, 2$), respectively [9]:

$$
\boldsymbol{a}_k = \sum_{k=1,2} \mu_k \left(\frac{\boldsymbol{r}(t) - \boldsymbol{r}_k(t)}{\|\boldsymbol{r}(t) - \boldsymbol{r}_k(t)\|} - \frac{\boldsymbol{r}_k(t)}{r_k(t)^3} \right) \quad (16)
$$

The positions of the sun and moon are obtained using the formulation from the Astronomical Almanac [9].

2. Nongravitational Perturbations

The acceleration due to aerodynamic drag can be obtained from the following equation [9]:

$$
\boldsymbol{a}_{\text{drag}} = -\frac{1}{2} \frac{c_D A}{m} \rho v_{\text{rel}} \boldsymbol{v}_{\text{rel}} \quad (17)
$$

where c_D is the drag coefficient; A is the satellite cross-sectional area normal to the incident flow; m is the spacecraft mass; ρ is the atmospheric density at the current position; and $\boldsymbol{v}_{\text{rel}}$ is the relative velocity of the satellite with respect to the atmosphere. The atmospheric density model used is the Drag-Temperature Model 2013 (DTM-2013), making use of the observed daily solar flux and geomagnetic activity indices [15]. Moreover, the Horizontal Wind Model 2014 (HWM14) is also incorporated to consider deviations in atmospheric winds from the assumption of a corotating atmosphere [16]. The historical value of 2.2 was chosen for c_D.

However, in our model, we refine the computation of aerodynamic drag by considering additional terms due to the velocity component of the spacecraft rotation with respect to the atmosphere and obtain a slightly modified equation for the aerodynamic drag. By dividing the spacecraft in tessellated surfaces defined by the three vertices and the unit inward surface normal $\boldsymbol{n}_p$, as shown in Fig. 1, the drag acceleration can be calculated as a sum over each triangular surface p in view of the relative wind as follows [11]:

$$
\boldsymbol{a}_{\text{drag}} = -\sum_p \frac{1}{2} \frac{c_D A_p}{m} \rho (\cos\alpha v_{\text{rel}} \boldsymbol{v}_{\text{rel}} + (\boldsymbol{n}_p^T(\boldsymbol{c}_p^\times \boldsymbol{\omega}_{\text{rel}}))\boldsymbol{v}_{\text{rel}}
$$
$$
- v_{\text{rel}} \cos\alpha \boldsymbol{c}_p^\times \boldsymbol{\omega}_{\text{rel}}) \quad (18)
$$

where A_p is the area of surface p; $\cos\alpha = -\boldsymbol{n}_p \cdot \boldsymbol{v}_{\text{rel}}/v_{\text{rel}}$; $\boldsymbol{c}_p$ is the position of the center of pressure of surface p from the center of mass; and $\boldsymbol{\omega}_{\text{rel}}$ is the relative angular velocity of the spacecraft with respect to the atmosphere. Surfaces are considered to be in view of the relative wind when $\cos\alpha > 0$.
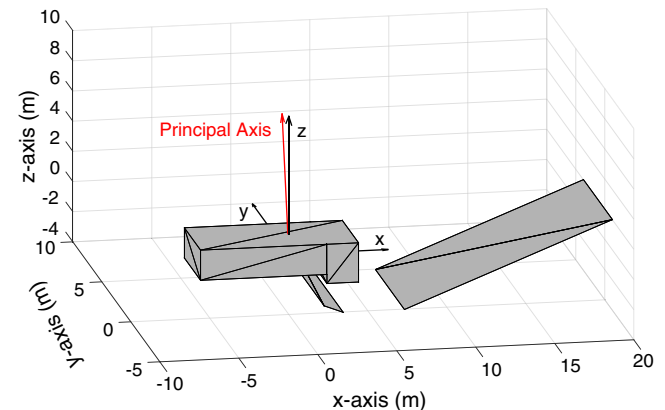

Fig. 1 Tessellated model of Envisat's surface geometry in the body-fixed frame.

The aerodynamic torque for a spinning spacecraft can then be calculated by computing a surface integral over the area of surface p and summing over all the exposed surfaces [11]:

$$\boldsymbol{\tau}_{\text{drag}} = -\sum_p \frac{1}{2} c_D \rho \left(v_{\text{rel}} A_p \cos \alpha \boldsymbol{c}_p^\times \boldsymbol{v}_{\text{rel}} + \iint_A (\boldsymbol{n}_p^T (\boldsymbol{r}_p^\times \boldsymbol{\omega}_{\text{rel}}))(\boldsymbol{r}_p^\times \boldsymbol{v}_{\text{rel}}) \, dA \right.$$
$$\left. - \iint_A v_{\text{rel}} \cos \alpha \boldsymbol{r}_p^\times \boldsymbol{r}_p^\times \boldsymbol{\omega}_{\text{rel}} \, dA \right) \quad (19)$$

where $\boldsymbol{r}_p$ is the position on the surface with respect to the body's center of mass. For a general spacecraft geometry model defined by triangular surfaces, an analytical solution to the surface integrals in Eq. (19) as a function of the positions of the three vertices is summarized in Appendix B.

Next, the eddy-current torque is a response of a spinning spacecraft body's conductive material to the Earth's magnetic field. The eddy-current torque can be calculated as follows:

$$\boldsymbol{\tau}_{\text{eddy}} = (\boldsymbol{M}\boldsymbol{\omega}^\times \boldsymbol{B})^\times \boldsymbol{B} \quad (20)$$

where $\boldsymbol{M}$ is the spacecraft's magnetic tensor as defined by [17], and $\boldsymbol{B}$ is the Earth's magnetic field. The value of $\boldsymbol{B}$ is calculated from the Earth's geomagnetic potential V, which is a function of the geocentric radius r, colatitude $\phi = 90° - \theta$, and longitude λ [9]:

$$\boldsymbol{B} = -\nabla V \quad (21)$$

$$V(r, \phi, \lambda) = a \sum_{n=1}^{k} \left(\frac{a}{r}\right)^{n+1} \sum_{m=0}^{n} (g_n^m \cos(m\lambda) + h_n^m \sin(m\lambda)) P_n^m[\cos\phi] \quad (22)$$

where $a = 6371.2$ km is the geomagnetic convention for Earth's mean reference spherical radius, g and h are Gauss coefficients from the International Geomagnetic Reference Field 12th Generation (IGRF-12), and P_n^m are the Schmidt normalized associated Legendre functions evaluated at $\cos\phi$ [18].

The next major external perturbation considered is the effect of solar radiation on the spacecraft surfaces. Similar to aerodynamic drag, the force associated with direct solar radiation can be calculated as a sum over every sunlit surface p [11]:

$$\boldsymbol{a}_{\text{solar}} = \sum_p \frac{\phi_s}{mc} \left[(\sigma_a + \sigma_{rd})\boldsymbol{s} + \frac{2}{3}\sigma_{rd}\boldsymbol{n}_p + 2\sigma_{rs}\cos\beta \boldsymbol{n}_p \right] A_p \cos\beta \quad (23)$$

where σ_a, σ_{rd}, and σ_{rs} represent the coefficients of absorption, diffuse reflection, and specular reflection for that surface, respectively; $c = 2.99792458 \times 10^8$ m·s^{-1} is the speed of light; ϕ_s is the solar radiation photon flux; $\boldsymbol{s} = -(\boldsymbol{r}_1/r_1)$ is the unit vector of the incident light direction, with $\boldsymbol{r}_1$ being the Earth–sun vector, as specified in Sec. II.A.1; and $\cos\beta = \boldsymbol{s} \cdot \boldsymbol{n}_p$. Surfaces are considered to be in view of the sun when $\cos\beta > 0$. The solar radiation photon flux varies with time and can be calculated as

$$\phi_s = \psi S_R \left(\frac{a_u}{r_1}\right)^2 \quad (24)$$

where $S_R = 1361$ W·m^{-2} is the solar radiation constant, $a_u = 1.495978707 \times 10^{11}$ m is the astronomical unit, and ψ is the Earth shadow function, which equals 0 when the satellite is in the Earth's shadow and 1 when the satellite is sunlit. A geometrical model of the penumbra transition when $0 < \psi < 1$ is used [19]. The torque associated with solar radiation can then be obtained from the acceleration derived previously and summed over every sunlit surface p [11]:

$$\boldsymbol{\tau}_{\text{solar}} = \sum_p \boldsymbol{c}_p \times m\boldsymbol{a}_{\text{solar},p} \quad (25)$$

Internal energy dissipation is the last torque included in the present model because its effect is known to be significant in the long-term attitude motion of spacecraft. Within the rigid-body modeling framework, a simple way to capture the effect of internal energy dissipation is by using a Kane damper [20]. This mechanism consists of a spherical mass contained inside a cavity full of viscous fluid at the spacecraft's center of mass. Assuming that the centers of mass of the spacecraft and the damper remain coincident, a torque proportional to their relative angular velocity will arise:

$$\boldsymbol{\tau}_{\text{damper}} = k_d(\boldsymbol{\omega}_d - \boldsymbol{\omega}) \quad (26)$$

where $\boldsymbol{\omega}_d$ is the angular velocity of the damper with respect to the inertial frame, expressed in the body-fixed frame, and k_d is a damping constant. The damper can be treated as a separate rigid body, with its own equations of motion, similar to Eqs. (2–4), but as a function of $\boldsymbol{\omega}_d$, $\boldsymbol{q}_d$, and $\boldsymbol{I}_d$, and with only $-\boldsymbol{\tau}_{\text{damper}}$ as an external torque.

Finally, hypervelocity impacts from small debris and micro-meteoroids can also be included using impact fluxes from the ESA MASTER-2009 software but were previously shown to have a negligible effect on both Envisat's orbit and attitude motion and were therefore excluded from this analysis [21–23].

B. Model Inputs

Because of the complexity of the model, various input parameters are required. These can be split into four categories: perturbation model parameters, spacecraft parameters, initial conditions, and propagation parameters. Those in the first grouping specific to the Envisat case study are presented in the previous section; however, not every perturbation was considered in the baseline scenario as defined in Table 2. In particular, the solar radiation torque has previously been shown to cause only a short-term periodic behavior in Envisat's angular velocity and no change in its secular evolution or on the spin axis motion [24]. Therefore, it was not considered in the baseline simulations; however, a deeper investigation is performed in Sec. III. Internal energy dissipation was similarly excluded in the baseline results, but simulations including it and varying the various parameters are also presented in Sec. III. In addition, we investigate the effects of dropping some of the terms in the aerodynamic torque as well as varying the order of the gravitational potential. Supplementary simulations and the corresponding results are all summarized in Table 2.

Spacecraft parameters include the spacecraft mass, inertia tensor, magnetic tensor, and spacecraft geometry. The spacecraft weight is taken as 7827.9 kg, and the following inertia and magnetic tensors are assumed [7,25]:

$$\boldsymbol{I} = \begin{bmatrix} 17023.3 & 397.1 & -2171.4 \\ 397.1 & 124825.7 & 344.2 \\ -2171.4 & 344.2 & 129112.2 \end{bmatrix} \text{kg} \cdot \text{m}^2 \quad (27)$$

$$\boldsymbol{M} = \begin{bmatrix} 931500 & 0 & 0 \\ 0 & 1059000 & 0 \\ 0 & 0 & 1059000 \end{bmatrix} \text{kg}^{-1} \cdot \text{m}^2 \cdot \text{s}^3 \cdot \text{A}^2 \quad (28)$$

It is interesting to note that, although not so in appearance, Envisat's inertial distribution is close to that of an axisymmetric body. The inertia tensor stated previously was determined directly by ESA, and because no damage to the spacecraft has been observed [6,25], we have high confidence in the inertial parameters used. However, the magnetic tensor was obtained by dividing the spacecraft into parts with assumed magnetic properties according to their structural materials [7] and, therefore, is subject to large uncertainty. The effect of this uncertainty is investigated in the next section.

Table 2   Influence of initial conditions and perturbation model parameters

Simulation	Parameter	Baseline	Change	Difference in angular motion
SS1	Aerodynamic drag	Included	Excluded	Negligible
SS2	Gravitational field	Order and degree 12	Order and degree 24	Negligible
SS3	Gravity-gradient torque	Order and degree 12	Order and degree 1	Negligible
SS4	Aerodynamic drag and torque	Full model	No spin terms	Negligible
SS5	Aerodynamic torque	Included	Excluded	Negligible
SS6	Torques considered	Gravity-gradient, eddy-current, aerodynamic	Only eddy-current	No precession, nutation or libration
SS7	Torques considered	Gravity-gradient, eddy-current, aerodynamic	Only gravity-gradient	Angular velocity, nutation and libration remain constant throughout propagation
SS8	Initial angular velocity magnitude	2.9 deg·s^{-1}	2.6 deg·s^{-1}	Nutation and libration period is proportionally ~10% smaller throughout propagation
SS9	Geomagnetic model	Thébault et al. [18]	Chulliat et al. [27]	Negligible
SS10	Magnetic tensor	Gómez and Walker [7]	Decreased by 10%	Angular velocity decrease is ~6% smaller
SS11	Initial angular velocity direction	Body-frame z axis	Major principal axis	No wobbling
SS12	Initial angular velocity direction	Body-frame z axis	Farther away from principal axis (initial wobbling amplitude 100% larger)	Wobbling amplitude 100% larger throughout propagation
SS13	Solar radiation pressure and torque	Excluded	Included	Evolution of angular velocity highly dependent on orientation of solar panel
SS14	Internal energy dissipation	Excluded	Included	Faster wobbling decrease
SS15	Time step	1 s	0.1 s	Negligible

The geometry, specifically the surface model, already introduced in Fig. 1, consists of a list of triangular surfaces, each defined by the position vectors of its three vertices and the unit inward surface normal, all in the body frame. As shown, Envisat's geometry is made up of 28 triangular surfaces. The model consists of the main satellite body ($10 \times 2.6 \times 2.8$ m), an antenna measuring (10×1.3 m), and a solar panel (14×5 m). The solar panel is locked, making a 22 deg angle with respect to the x–y plane [26]. The body frame axes are shown in black in Fig. 1 whereas the maximum principal axis of inertia is shown in red, defined by the direction vector $[-0.0190 \quad 0.0771 \quad 0.9968]^T$ in the body frame. It is rotated approximately -4.5 deg from the z axis about the x axis.

The initial orbital conditions consist of the orbit and epoch, which are obtained from a TLE for the desired object and then converted into a set of osculating orbital elements using the SGP4 propagator [10]. The initial attitude conditions are needed as well: the orientation of the spacecraft in the orbital reference frame,[‡] which is then rotated to the inertial frame, and the initial angular velocity vector in the body frame, shown in Fig. 1. Because Envisat experienced an unexplained spin-up after contact was lost, the initial conditions were set to a TLE obtained after this event occurred. The following TLE, from 7 May 2013, was used as input:

```
1  27386U 02009A   13127.45641789  .00000089  00000-0  44087-4 0  3555
2  27386  98.4303 196.5510 0001204  87.6383 272.4946 14.37606880585289
```

At the TLE epoch, from observations that will be reviewed in the Sec. IV, Envisat is estimated to be rotating at approximately 2.9 deg·s^{-1} or, equivalently, having a rotation period of 125 s. For comparison, the satellite's orbital period at that time is approximately 100 min. From observations, it is also widely accepted that Envisat is spinning in retrograde motion (opposite to its orbital motion), with its rotation axis approximately parallel to the symmetry axis of its retroreflector panel, which in turn is close to the satellite's maximum principal axis of inertia [4]. Envisat's initial angular velocity vector was therefore assumed to be along the body-frame z axis (see Fig. 1).

The initial orientation of the body was parameterized by the initial orientation of the angular velocity vector with respect to the negative

orbital normal vector. Because no information exists on the exact attitude of the spacecraft for the epoch of the simulation, the baseline scenario for the propagation was chosen to have the initial angular velocity vector 30 deg away from the negative orbit normal. To explicitly characterize the motion of the spin axis and shed light on contradictions in current literature regarding this issue, various additional simulations were performed. Specifically, five simulations were run by varying the initial inclination of the angular velocity vector, always lined up with the body-frame z axis, from the negative orbit normal as 0, 8.5, 17, 28, and 45 deg. With the exception of 45 deg case, the other values correspond to the results deduced from observations and were chosen to provide a comparison to previous studies which will be presented in Sec. IV. Three supplementary scenarios related to the variation of initial angular velocity (magnitude and direction) were also investigated as per Table 2.

Finally, the propagation parameters involved are the duration of the propagation and the time step used in the numerical integration. For all propagation scenarios, the duration was set to four years (1461 days) with a time step of 1 s. This time step was considered to be sufficiently small because only a 0.12% energy loss was found after checking the energy–work balance throughout the simulation. A propagation with a time step of 0.1 s was also performed, and the differences in the obtained results were found to be negligible.

III. Propagation Results

A. Analysis of Baseline Propagation Results

The rotational motion of Envisat is very complex, but significant insight can be gained by considering the evolution of the angular momentum and angular velocity of the satellite. Analysis of simulation results reveals three distinct angular motions that can be observed in the inertial frame, as shown in the schematic, not to scale, in Fig. 2: 1) a precession of the angular momentum vector (in purple), about the Earth's rotation axis (in green), as the orbital plane precesses; 2) a revolution of the angular momentum vector about the orbit normal (in red), composed of a nutation and a libration with locked periods; and 3) a wobbling of the angular velocity vector (in pink), about the body's angular momentum vector. The direction of each motion and of the spacecraft rotation are also shown. The precise definitions of the aforementioned motions employed in this work are stated as follows,

---

[‡]The orbital frame definition employed in this study assumes that the x_O axis is in the direction of motion, and z_O points toward Earth in the orbital plane.
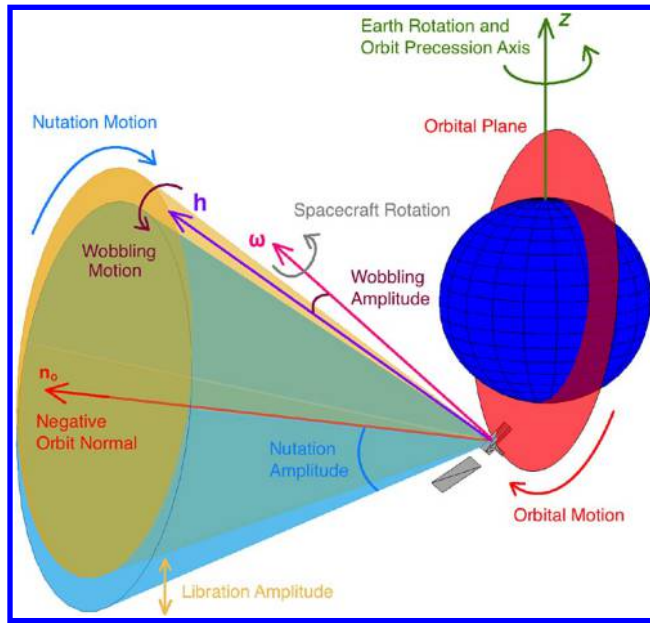
Fig. 2 Schematic of angular motions experienced by Envisat.

making use of the angular momentum frame§ and the orbital precessing frame.¶

Definition 1: A precession is a secular change in the first Euler angle of the 3-1-3 attitude parameterization of the angular momentum frame with respect to the inertial frame.
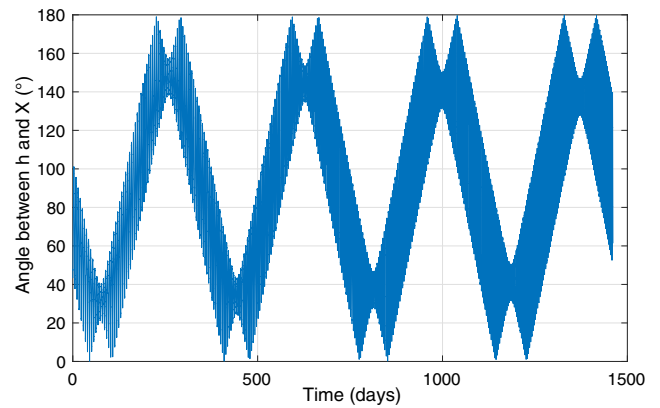
Definition 2: A nutation is a secular change in the first Euler angle of the 3-1-3 attitude parameterization of the angular momentum frame with respect to the orbital precessing frame.

Definition 3: A libration is an oscillation of the second Euler angle of the 3-1-3 attitude parameterization of the angular momentum frame with respect to the orbital precessing frame. In this study, the corresponding angle is defined as the nutation amplitude.

Definition 4: Wobbling denotes the torque-free motion of the angular momentum vector about the angular velocity vector for an inertially asymmetric body.
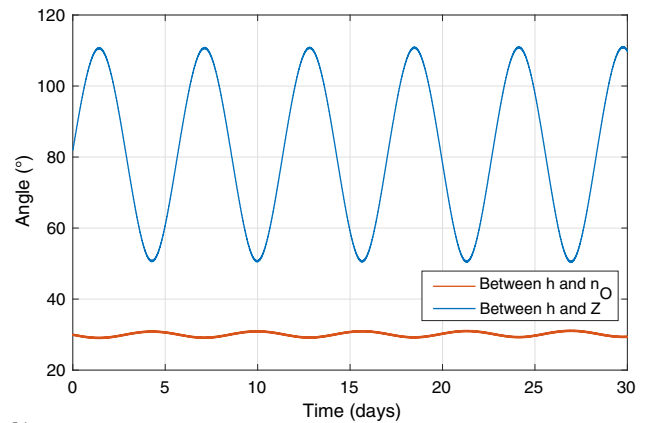
The three angular motions were determined by comparing the satellite's angular momentum vector $h = I\omega$ to the inertial X axis, the inertial Z axis, the negative orbit normal n_O, and the angular velocity vector ω. Figure 3 displays the relevant angular distance measures for the appropriate time durations for the baseline scenario. From the secular change in the minimum angle between h and X over the four-year propagation, as seen in Fig. 3a, the precession of Envisat's angular momentum vector can be deduced. It has a period of approximately one year as it follows the orbital plane's precession. It is the gravity gradient torque that fixes the motion of the angular momentum vector with and about the orbit normal. The high-frequency oscillations seen in Fig. 3a represent the rotation of the angular momentum vector with respect to the orbit normal (nutation and libration), which quickens and widens over time.

The second motion is the rotation of the angular momentum vector with respect to the orbit normal. Figure 3b shows the h–Z and h–n_O angles over the first month of the propagation. The h–Z angle isolates the nutational motion; from its oscillations, the nutation period and amplitude can be deduced. Similarly, the evolution of the h–n_O angle allows to separate out the libration motion, and the libration period and amplitude can be derived. One can see that the libration and nutation periods are exactly the same. This motion is also due to the gravity gradient torque.
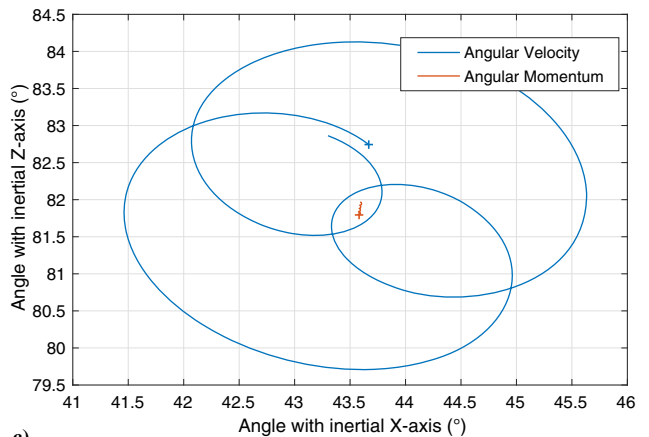
The third motion is the wobbling motion of the angular velocity vector ω around the angular momentum vector. Figure 3c shows this

---

§The angular momentum frame definition employed in this study assumes that the z_h axis is fixed with the body's angular momentum vector.

¶The precessing frame definition employed in this study assumes that the z_P axis is in the direction of the negative orbit normal n_O, and x_P points toward the orbit's precessing ascending node.

a)

b)

c)

Fig. 3 Examples of the evolution of Envisat's angular motions for the baseline scenario.

motion from a sample 258 s of the simulation (approximately one wobble period). The amplitude of the wobbling, measured as the maximum angular deviation between h and ω, is approximately 2 deg in this case. This motion is due to the fact that the initial angular velocity is not aligned with the principal axis of inertia of the spacecraft.

Figure 4 shows the evolution of Envisat's angular velocity magnitude (spin rate), nutation period and amplitude, libration amplitude, and wobbling period and amplitude, for the five simulations corresponding to the five initial inclinations of ω stated earlier. Multiple observations can be made from the simulations on the tendencies of these motions. First, the decay of the angular velocity magnitude due to the eddy-current torque is present, as noted previously [7]. Second, the amplitude of the nutation increases consistently in every case, whereas the period decreases over the four-year propagation. Third, the libration and nutation periods, which are on the order of days, are locked together throughout the propagation and are longer for larger nutation amplitudes. Fourth, a larger initial deviation from the negative orbit normal (nutation amplitude) produces a slower decay of angular
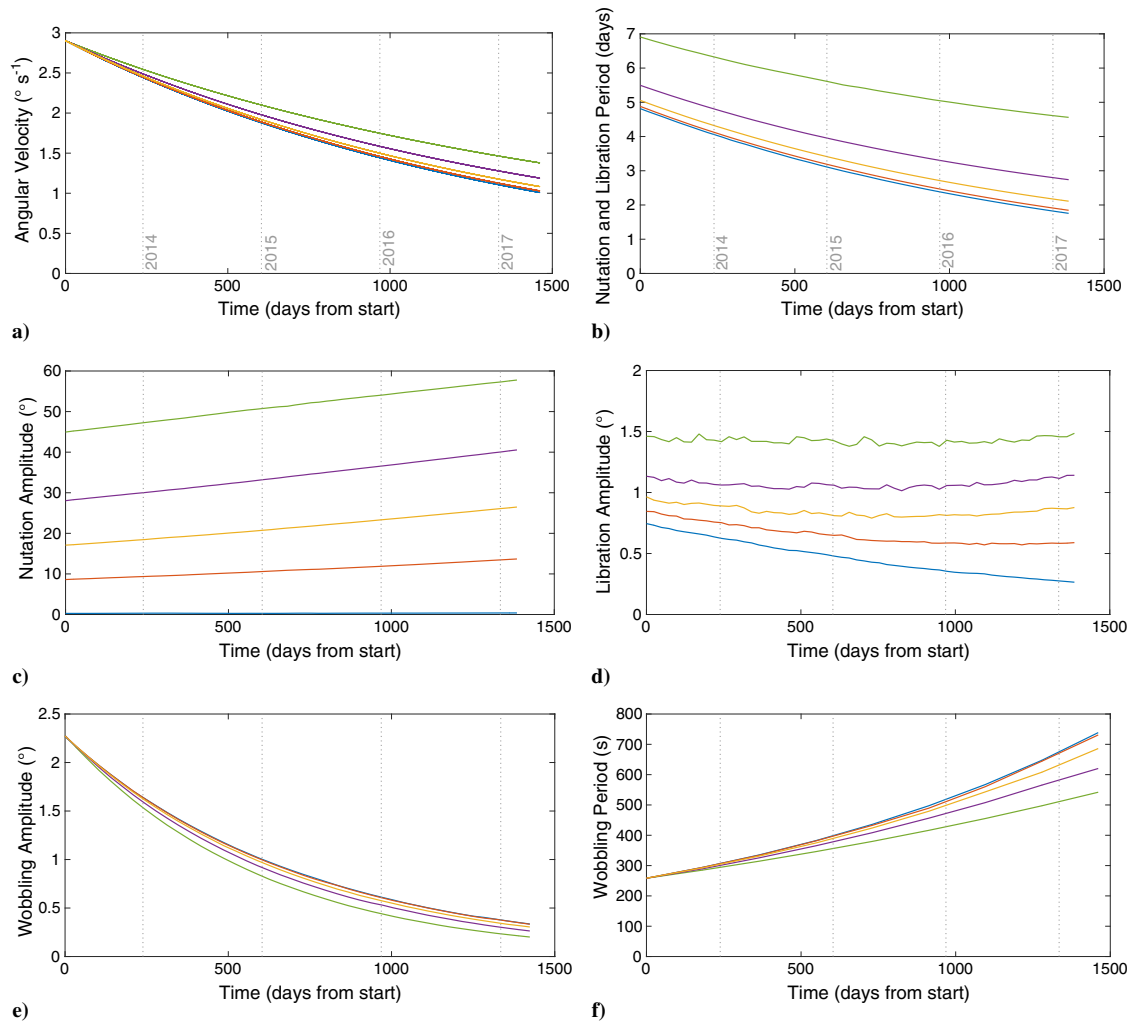
Fig. 4   Evolution of Envisat's angular motion throughout the four-year propagation.

velocity. Fifth, the larger the nutation is, the larger the libration amplitude is as well. It is interesting to note that, unless the rotation starts out perfectly about the axis perpendicular to the orbital plane (i.e., the 0 deg case), the nutation motion will become larger and quicker; an increase in the amplitude of approximately 50% occurs after four years, for the cases where the initial angular velocity vector is 8.5 and 17 deg from the negative orbit normal, whereas the period decreases by a factor of 2.5 after four years, from approximately 5 to 2 days. Furthermore, in each case, the wobbling amplitude decreases to below 0.5 deg, approaching a major principal axis spin, with a larger decrease for the cases where the initial spin axes are farther away from the negative orbit normal. The wobbling slows down the quickest (200% increase of the period in four years) for the case when the angular velocity vector is perpendicular to the orbital plane.

B.   Sensitivity Study on Input Parameters

Although these results demonstrate that the expected wobbling motion is small and simulations have shown that it becomes smaller and slower with time, the nutation of Envisat's angular momentum vector is expected to become larger and faster with time, which could be worrying for future ADR missions. Nevertheless, the dependence of these results on the model parameters and initial conditions needs to be explored further.

Table 2 displays the supplementary simulations (SS) that were carried out by varying the indicated model parameters and initial rotation from the baseline scenario. First and foremost, it was found that the evolution of Envisat's orbital motion has a negligible effect on the rotational motion results; aerodynamic drag and third-body gravitational perturbations showed almost no influence on the evolution of Envisat's angular motion (SS1), and neither did increasing the degree

and order of the gravitational potential model from 12 to 24 (SS2). It was also shown that, in this case, not considering higher-order terms in the calculation of the gravity-gradient torque was negligible, at least when analyzing the motion of the spin axis (SS3). Excluding the extra terms in the aerodynamic torque and drag for a spinning spacecraft did not reveal any changes (SS4), and neither did excluding the aerodynamic torque completely (SS5); however, as expected, removing either the gravity-gradient torque (SS6) or the eddy-current torque (SS7) led to significant differences, showing that they are indeed the dominating torques. In this light, the influence of the relevant parameters for these two torques was investigated further.

Reducing the initial angular velocity magnitude by approximately 10% led to a similar decrease of the nutation/libration period throughout the propagation (SS8). This occurs as the spin stabilization of the spacecraft weakens for a slower spin rate, thus amplifying the effect of the gravity gradient torque. No other change in the angular motion was found. Using the World Magnetic Model for the geomagnetic model [27] instead of IGRF-12 did not reveal any differences (SS9), but decreasing the magnetic tensor values by 10% led to a slower decrease of the spin rate after four years by approximately 6% (SS10). These simulations have shown that the precession, nutation, and libration motions due to the gravity-gradient torque persist regardless of the initial spin conditions, although the period of the nutation and libration depends on the angular velocity magnitude. Moreover, the spin rate decay due to the eddy-current torque was shown to be the cause of the evolution of the amplitude and period of these motions. Finally, the extent of the wobbling motion was found to only depend on the initial difference between the maximum principal axis and the spin axis direction, although its damping toward the major-axis spin will occur with time (SS11 and SS12).

As previously mentioned, the effect of solar radiation was excluded from the baseline scenario because it had been shown to cause only a short-term periodic behavior in angular velocity for Envisat [24]. However, the effect of solar radiation on the spin characteristics of satellites is known to be highly dependent on the shape of the spacecraft and the optical properties of its surfaces; more specifically, the position and orientation of the solar panel can have a large influence on the evolution of a satellite's angular velocity [28]. Although Envisat was seen to have its solar panel in a position close to the way presented in Fig. 1, its exact rotation about the x axis is difficult to determine, and it could vary by a few degrees [26]. Multiple simulations were carried out, for small changes of the orientation of the solar panel, by rotating it about the body-frame x axis (SS13). The solar panel optical coefficients were taken from the International DORIS Service macromodel for Envisat [29].

Figure 5a shows the evolution of the angular velocity magnitude for the simulations where the solar panel was rotated by −10 to 5 deg about the x axis, with an increment of 1 deg. The black line represents the baseline scenario without solar radiation. As can be seen, even a small change can cause a large difference in the evolution of angular velocity. From Fig. 5, it was found that the most likely orientation of the solar panel is in such a way that its surface normal points toward the satellite's major principal axis, which occurs when the solar panel is rotated between −4 and −5 deg about the x axis (recall that the maximum principal axis, as shown in red in Fig. 1, is inclined by approximately −4.5 deg). Any deviation from this by even 1 deg causes a significant, unrealistic change in the evolution of angular velocity. Adding solar radiation did not reveal any changes in the evolution of the nutation and wobbling amplitudes for the −4 and −5 deg cases, although the period of each motion did change, evolving proportionally to angular velocity. The libration amplitude showed a noticeable difference: an oscillation with a period of one year and an amplitude of approximately 0.1 deg on top of its secular evolution, as exhibited in Fig. 5b, when adding solar radiation with the solar panel rotated at −4 and −5 deg.

Finally, including internal energy dissipation was also investigated (SS14). Multiple cases were analyzed; the moment of inertia I_d was varied between 1 and 10 kg · m², and damping constants from 0.01 to 1 kg · m² · s⁻¹ were considered. No effects on the motion of the spin axis or angular velocity of the spacecraft were found, apart from a faster decrease of the wobbling motion (i.e., a faster convergence to a major-axis spin). Depending on the input parameters of the damper, the wobbling motion died down after 100 days to 3 years, bringing the spacecraft to a pure major-axis spin. Figure 5c shows such a decay in the wobbling amplitude for both the fastest and slowest decay seen from the simulations performed.

IV. Review of Observational Results

Envisat was launched in March 2002 into a sun-synchronous polar orbit at an altitude of 772 km as an Earth observation satellite. ESA lost contact for yet unknown reasons in April 2012 and declared the end of mission a month later. The spacecraft subsequently experienced
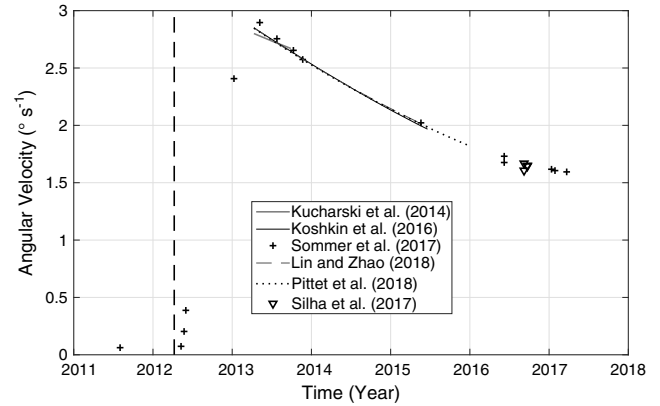

Fig. 6 Reproduction of Envisat's angular velocity estimates as a function of time from observational studies.

a spin-up, also unexplained, followed by a decay of its rotational energy, found to be due to the eddy-current torque [4,7,25]. Three observation methods have been used to estimate Envisat's rotational motion: satellite laser ranging, photometric measurements, and ISAR images. Figure 6 and Table 3 provide an overview of observational results to date that have dealt with Envisat's angular velocity and attitude motion. The vertical dashed line in Fig. 6 represents the time of loss of contact. The studies obtained estimates over different but overlapping time frames using various methods. A good agreement on the observed decrease of the spacecraft's angular velocity magnitude from May 2013 onward exists, which is also in line with the simulation results presented in Fig. 4a. However, four majors sources of uncertainty are present in our simulation results that would lead to differences in the rate of decay of angular speed: the initial orientation of ω, the initial angular speed (SS8), the value of the magnetic tensor (SS10), and the orientation of the solar panel (SS13). Taking these into account, the observed angular velocity evolution agrees well with simulation results. Nevertheless, large differences in the motion of the spin axis have been observed, and contradictions related to its stability are abundant. Moreover, some studies made certain assumptions to estimate Envisat's inertial angular velocity magnitude and spin axis direction, and uncertainty in these estimates is rarely discussed in detail. A review of all the measurements made thus far, taking into account knowledge obtained from our simulation results, is therefore timely and crucial.

Some satellites, including Envisat, contain retroreflectors that can be used for satellite laser ranging. SLR residuals, defined as the difference between the laser range measured from the observatory on Earth to the retroreflector array (RRA) onboard the satellite and the predicted position of the satellite's center of mass with respect to the observatory, therefore provide a signal measuring the motion of the RRA as the spacecraft rotates around its center of mass [4]. From oscillations in SLR residuals, an estimate of the satellite's apparent spin period as measured from the observatory can be obtained [4].
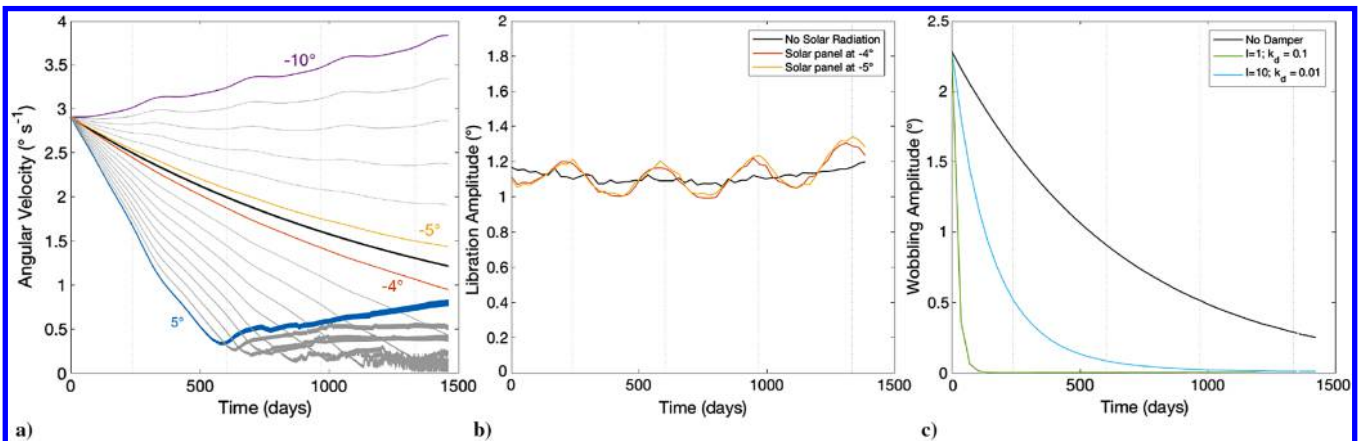

Fig. 5 Evolution of Envisat's angular motions for supplemental simulations.

Table 3   Summary of Envisat angular motion studies

Study	Time frame	Method	Information relevant to spin axis orientation
Shakun et al. [32]	April–Aug. 2013	Light curves	Concluded that a precession of the spin axis is present
Kucharski et al. [4]	April–Sept. 2013	SLR	Spin axis inclined 28 deg from $\boldsymbol{n}_O$ and fixed in the orbital frame over entire period
Koshkin et al. [5]	2013–2015	Light curves	Assumed a fixed spin axis in orbital frame and concluded that it to be aligned with $\boldsymbol{n}_O$
Silha et al. [34]	Sept. 2016	Combination	Spin axis orientation obtained directly from ISAR images for each pass
Sommer et al. [6]	2011–2017	ISAR	Large spread in spin axis orientation is observed over the entire time frame
Lin and Zhao [33]	2013–2015	Light curves	Included spin axis motion from gravity-gradient torque; concluded that spin axis is nutating at 8.5 deg from $\boldsymbol{n}_O$; found presence of evolving nutation period (4.8 to 3.4 days from 2013 to 2015) and libration amplitude (0.7 to 0.5 deg)
Pittet et al. [30]	2013–2015	SLR	Spin axis orientation obtained for each pass and concluded fixed in precessing frame at 17 deg from $\boldsymbol{n}_O$

Such measurements can only be taken when the satellite pass over the observatory is long enough relative to its rotation period so that such oscillations are observable and when the RRA is visible to the ground station. To obtain the inertial spin parameters of the satellite, various methods can be used.

Some of the first postmission observations dedicated to understanding what happened to Envisat were obtained by the International Laser Ranging Service at the request of ESA throughout 2013 [4]. From an analysis of 87 passes from various SLR stations, the campaign results obtained estimates of the apparent spin period of the satellite and determined that Envisat was witnessing a slow decrease of its angular velocity. The inertial spin periods were then obtained by assuming a specific spacecraft orientation. From the entire set of 347 passes during the seven-month period, the spacecraft's spin axis was determined to be fixed in the orbital frame, inclined at approximately 28 deg from the negative orbit normal and perpendicular to the spacecraft velocity direction [4]. Observations from 46 passes seen by the Glaz SLR station having a mean duration of 6.8 min were then used to estimate the inertial spin period of the satellite by assuming it was spinning opposite to its orbital motion (in retrograde motion). The spin axis orientation was assumed to be fixed in the orbital reference frame over the seven-month period, meaning that a precession is considered and that a nutation equal to the orbital period of 100 min was assumed. However, simulation results for the 28 deg initial orientation of the spin axis with respect to the orbit normal (purple scenario in Fig. 4) show that this is impossible because a nutation motion with period of a few days is expected in this case. Furthermore, if the assumed orientation of the spin axis is incorrect, an error on the inertial spin period will follow [4].

A more recent study dealing with SLR observations determined Envisat's spin parameters using SLR residuals from each single pass, instead of fitting over multiple passes [30]. Using the data from 31 passes observed from the Zimmerwald SLR station throughout 2013–2015, the study concluded that Envisat's spin axis was aligned with its principal axis of inertia and that it made a fixed 17 deg angle with the negative orbit normal, disregarding the possibility of a nutation, which again contradicts our simulation results (yellow scenario in Fig. 4). However, the conclusion in [30] should be taken lightly because a large spread of the spin axis orientation over the 2.5 year time frame is present in the results shown.**

The second method that has been applied to study Envisat's angular motion is light curve measurements obtained from variations of the target's brightness as seen from a ground telescope. From repeated peaks in the measurements, one can, in a way similar to SLR measurements, obtain an estimate of the apparent spin period of the target [31]. Converting to the inertial spin period, however, requires more care than doing so from SLR residuals because a direction of the spin axis orientation cannot be obtained directly. Difficulties first exist to correctly obtain corresponding light peaks for slowly rotating spacecraft where the reflection geometry as seen from the ground changes from one peak to the next over one pass [5]. An assumption that the light reflections come from smooth flat surfaces and that the

spin axis is fixed over one pass is also made to obtain valid inertial spin period values. Our results indicate that the latter is indeed a reasonable assumption for a short (few minutes) pass.

First results from light curves were obtained using the KT-50 telescope, and it was concluded from various observations ranging from April to August 2013 that, because of the spread of inertial spin period values, fluctuations of the spin axis orientation were present, and a precession of the spin axis with the orbital plane was deduced [32]. More sets of results were also obtained from the same telescope for the period from April 2013 to May 2015. The inertial spin periods were derived by assuming that the actual attitude state can be determined by minimizing the spread of the resulting inertial spin period points; an assumption on the motion of the spin axis over the entire time frame is therefore made [5]. After assuming that the spin axis was fixed in the orbital frame and testing several inclinations of the spin axis with respect to the negative orbit normal from 0 to 30 deg, the study determined that the 0 deg case provided the best fit (i.e., that the spin axis orientation was along the negative orbit normal) [5]. Once more, the assumption that the spin axis is fixed in the orbital frame is more than likely incorrect. If the spin axis is indeed aligned with the negative orbit normal, our 0 deg simulation results (blue scenario) confirm that the spin axis should be fixed in the orbital frame; however, as the gravity-gradient torque forces a rotation of the angular momentum vector about the negative orbit normal, an average best fit of 0 deg would also provide the smallest spread in the inertial spin period estimates.

A later study included the analytical expression for the gravity-gradient torque in the model employed to convert from the apparent to the inertial spin period values [33] and therefore included the possibility of a nutation and libration, although no wobbling motion was considered. A best fit was found when the angular momentum vector made approximately an 8.5 deg angle with the negative orbit normal; for that nutation amplitude, the nutation period (locked with the libration period) was found analytically to decrease from 4.8 days in 2013 to 3.4 days in 2015, and the libration amplitude decreased from 0.7 deg in 2013 to 0.5 deg in 2015. These values are in approximate agreement with what was found in our simulation as shown in Fig. 4 (orange scenario). Nevertheless, our results clearly show that the reduction of the spin rate, confirmed by all observations to date, goes hand in hand with an increase in the nutation amplitude over time; however, there is no indication of evolution of the nutation amplitude in [33]. Including the gravity-gradient torque in the fitting model reduced the spread of the inertial spin period points as compared to the results in [5], but not to the level of measurement errors stated [5]. The source of this discrepancy is still unexplained, but a significant wobbling and the evolution of the nutation amplitude as predicted by our simulations may contribute to an explanation.

Inverse synthetic aperture radar (ISAR) imaging can also be used to determine the attitude state of a satellite in a more direct way than the other two methods. From multiple images obtained over a pass, a value for the angular velocity vector (magnitude and direction) can be deduced. The Tracking and Imaging Radar (TIRA) has focused on Envisat for multiple passes ranging from August 2011 to January 2017 [6]. During all of these observations, no specific motion of the spin axis is observed, and to the contrary, a large change in the spin axis direction can be seen in the inertial frame. The presence of the

---

**The distribution of observations in [30] indicates a spread of the spin axis orientation inclined from 5 to 35 deg from the negative orbit normal with error bars between 1 and 12 deg; the distribution of the azimuth of the spin axis in the reference frame fixed with the orbital plane oscillates from 90 to 315 deg, with much smaller error bars.

precession is witnessed, but a large nutation would also be needed to explain the spread in spin axis direction described.

Finally, these three methods have been used in conjunction: a study looking at four passes in September 2016 (two on the 6th and two on the 21st) determined inertial spin periods from both light curve measurements and SLR residuals from the ZIMLAT telescope assuming a fixed rotation vector over one pass obtained by TIRA images [34]. A conclusion that Envisat's spin axis orientation was constant was made, although a 10 deg difference between two vectors on consecutive passes 100 min apart and a 24–34 deg difference between both days were observed. The fixed orientation concluded from these results is therefore debatable. Even though the two sets of passes are two weeks apart, the orbit's precession does not entirely explain the difference, which strongly suggests that a nutation is present.

V. Conclusions

From the development of a novel and comprehensive coupled orbit-attitude propagation model and its application to the defunct satellite Envisat, insights into the evolution of its rotational motion have been obtained. Its complex attitude dynamics has been found to be composed of three distinct angular motions: 1) a precession of the satellite's angular momentum vector with the orbital plane; 2) a revolution of its angular momentum vector about the orbit normal, composed of a nutation and libration with locked periods on the order of a few days and decreasing and with the amplitude still uncertain; and 3) a wobbling of the angular velocity vector about angular momentum vector, although simulations have shown that any wobbling present after the satellite's spin-up has most likely decayed, leaving Envisat in a major-axis spin.

The three observation methods employed to date for estimating the rotation of Envisat are quite different but complementary: satellite laser raging (SLR) residuals can be used to determine both the spin rate and spin axis orientation over a single pass; photometric measurements will provide a continuous light signal from the satellite, from which a spin rate can be obtained; inverse synthetic aperture radar (ISAR) images will detect the instantaneous attitude of the satellite, and with multiple consecutive images, the spin rate and spin axis orientation can be determined. Although many of the observational studies to date using these three methods have concluded a fixed orientation of Envisat's spin axis in the inertial frame or orbital frame, the present analysis of the procedures used and data obtained shows that this is highly unlikely. Unless the spin axis is perfectly aligned with the orbit normal, an evolving nutation motion

will be due to a nutation of the spin axis. The present recommendations to obtain better estimates of Envisat's actual attitude motion are twofold. First, the attitude models used to obtain inertial spin period points from SLR measurements and light curves should include the possibility of a nutation and libration, as has previously been done for light curves, but should also allow for the evolution of the nutation amplitude. Second, to characterize these motions and fit simulation results with observations, a much larger observational data set is required on the time scale of each motion. Obtaining estimates for the nutation amplitude and period and their evolution with time could be done by analyzing SLR and inverse synthetic aperture radar data, first for multiple consecutive passes over a few days from various ground stations, and then by repeating these measurements several months later to detect their evolution.

The simulation results obtained from this study have provided multiple novel insights into Envisat's attitude motion in addition to the presence of the three angular motions. The derived high-order gravity-gradient torque and the complete formulation of the aerodynamic drag and torque for a spinning spacecraft were shown to be negligible for Envisat. Solar radiation was found to potentially have a large influence on the satellite, but when comparing to observations, it was deduced that the orientation of the solar panel was in such a way that its effect is minimal. Most importantly, the simulated nutation motion was shown to become larger and faster with time. As Envisat's rotation slows down, its relative spin stabilization effect will decrease, which will lead the gravity gradient torque and other environmental torques to push the satellite toward an even larger tumbling motion. Although Envisat's angular velocity magnitude is decreasing, this phenomenon indicates potential difficulties for the European Space Agency's upcoming e.Deorbit mission.

Appendix A: Gravity-Gradient Torque Partial Derivatives

The multiplicative matrices used in the derivation of the gravity-gradient torque presented in Sec. II.A.1 as a function of the position vector in the inertial reference frame $\boldsymbol{r} = [\, r_I \quad r_J \quad r_K \,]^T$ are

$$\frac{\partial^2 r}{\partial \boldsymbol{r}^2} = -\frac{1}{r^3} \begin{bmatrix} r_I^2 - r^2 & r_I r_J & r_I r_K \\ r_I r_J & r_J^2 - r^2 & r_J r_K \\ r_I r_K & r_J r_K & r_K^2 - r^2 \end{bmatrix} \tag{A1}$$

$$\frac{\partial^2 \theta}{\partial \boldsymbol{r}^2} = \frac{1}{r^4 (r_I^2 + r_J^2)^{3/2}} \begin{bmatrix} r_K(2r_I^4 + r_I^2 r_J^2 - r_J^4 - r_J^2 r_K^2) & r_I r_J r_K(3r_I^2 + 3r_J^2 + r_K^2) & -r_I(r_I^2 + r_J^2)(r_I^2 + r_J^2 - r_K^2) \\ r_I r_J r_K(3r_I^2 + 3r_J^2 + r_K^2) & r_K(-r_I^4 + r_I^2 r_J^2 - r_I^2 r_K^2 + 2r_J^4) & -r_J(r_I^2 + r_J^2)(r_I^2 + r_J^2 - r_K^2) \\ -r_I(r_I^2 + r_J^2)(r_I^2 + r_J^2 - r_K^2) & -r_J(r_I^2 + r_J^2)(r_I^2 + r_J^2 - r_K^2) & -2r_K(r_I^2 + r_J^2)^2 \end{bmatrix} \tag{A2}$$

due to the gravity gradient torque will occur, contrary to what has been concluded thus far. An agreement on the precession of the spin axis with the orbit seems to exist, but the presence of a nutation about the negative orbit normal and its time dependence needs to be acknowledged. The spread in the observed spin axis orientation, as determined by ISAR imaging and SLR, and the spread in the inertial spin periods from both SLR and light curves, even after considering the gravity gradient torque, show that such an evolving motion exists.

Characterizing this motion, however, is difficult, due to the complexity of such an angular motion and the scarcity of observations. However, any large motion observed after a few years

$$\frac{\partial^2 \lambda}{\partial \boldsymbol{r}^2} = \frac{1}{(r_I^2 + r_J^2)^2} \begin{bmatrix} 2r_I r_J & r_J^2 - r_I^2 & 0 \\ r_J^2 - r_I^2 & -2r_I r_J & 0 \\ 0 & 0 & 0 \end{bmatrix} \tag{A3}$$

$$\frac{\partial r}{\partial \boldsymbol{r}} \left(\frac{\partial r}{\partial \boldsymbol{r}} \right)^T = \frac{1}{r^2} \begin{bmatrix} r_I^2 & r_I r_J & r_I r_K \\ r_I r_J & r_J^2 & r_J r_K \\ r_I r_K & r_J r_K & r_K^2 \end{bmatrix} \tag{A4}$$

$$\frac{\partial \theta}{\partial \boldsymbol{r}}\left(\frac{\partial \theta}{\partial \boldsymbol{r}}\right)^T = \frac{1}{r^4(r_I^2 + r_J^2)}$$
$$\times \begin{bmatrix} r_I^2 r_K^2 & r_I r_J r_K^2 & -r_I r_K(r_I^2 + r_J^2) \\ r_I r_J r_K^2 & r_J^2 r_K^2 & -r_J r_K(r_I^2 + r_J^2) \\ -r_I r_K(r_I^2 + r_J^2) & -r_J r_K(r_I^2 + r_J^2) & (r_I^2 + r_J^2)^2 \end{bmatrix}$$

(A5)

$$\frac{\partial \lambda}{\partial \boldsymbol{r}}\left(\frac{\partial \lambda}{\partial \boldsymbol{r}}\right)^T = \frac{1}{(r_I^2 + r_J^2)^2} \begin{bmatrix} r_J^2 & -r_I r_J & 0 \\ -r_I r_J & r_I^2 & 0 \\ 0 & 0 & 0 \end{bmatrix}$$ (A6)

$$\frac{\partial r \partial \theta^T}{\partial \boldsymbol{r} \partial \boldsymbol{r}} + \frac{\partial \theta \partial r^T}{\partial \boldsymbol{r} \partial \boldsymbol{r}} = \frac{1}{r^3 \sqrt{r_I^2 + r_J^2}}$$
$$\times \begin{bmatrix} -2r_I^2 r_K & -2r_I r_J r_K & r_I(r_I^2 + r_J^2) - r_I r_K^2 \\ -2r_I r_J r_K & -2r_J^2 r_K & r_J(r_I^2 + r_J^2) - r_J r_K^2 \\ r_I(r_I^2 + r_J^2) - r_I r_K^2 & r_J(r_I^2 + r_J^2) - r_J r_K^2 & 2r_K(r_I^2 + r_J^2) \end{bmatrix}$$

(A7)

$$\frac{\partial r \partial \lambda^T}{\partial \boldsymbol{r} \partial \boldsymbol{r}} + \frac{\partial \lambda \partial r^T}{\partial \boldsymbol{r} \partial \boldsymbol{r}} = \frac{1}{r(r_I^2 + r_J^2)} \begin{bmatrix} -2r_I r_J & r_I^2 - r_J^2 & -r_J r_K \\ r_I^2 - r_J^2 & 2r_I r_J & r_I r_K \\ -r_J r_K & r_I r_K & 0 \end{bmatrix}$$ (A8)

$$\frac{\partial \lambda \partial \theta^T}{\partial \boldsymbol{r} \partial \boldsymbol{r}} + \frac{\partial \theta \partial \lambda^T}{\partial \boldsymbol{r} \partial \boldsymbol{r}} = \frac{1}{r^2(r_I^2 + r_J^2)^{3/2}}$$
$$\times \begin{bmatrix} 2r_I r_J r_K & r_K(r_J^2 - r_I^2) & -r_J(r_I^2 + r_J^2) \\ r_K(r_J^2 - r_I^2) & -2r_I r_J r_K & r_I(r_I^2 + r_J^2) \\ -r_J(r_I^2 + r_J^2) & r_I(r_I^2 + r_J^2) & 0 \end{bmatrix}$$ (A9)

Appendix B: Evaluation of Surface Integrals in Aerodynamic Torque Computation

The following will solve analytically the two surface integrals in Eq. (19), which are a function of the position of the three vertices of each triangular surface defining the spacecraft geometry model. Consider a triangular surface A defined by the position of its three vertices, $\boldsymbol{r}_1 = [x_1 \ y_1 \ z_1]^T$, $\boldsymbol{r}_2 = [x_2 \ y_2 \ z_2]^T$, and $\boldsymbol{r}_3 = [x_3 \ y_3 \ z_3]^T$. Its unit normal vector is given, defined by $\boldsymbol{n} = [n_x \ n_y \ n_z]^T$. Evaluating a function $f(x, y, z)$ over A can be simplified to

$$\iint_A f(x, y, z) \, dA = \iint_D f(x, y, z(x, y)) \sqrt{\left(\frac{\partial z}{\partial x}\right)^2 + \left(\frac{\partial z}{\partial y}\right)^2 + 1} \, dy \, dx$$ (B1)

where D is the projection of A on the x–y plane, and $z(x, y)$ can be defined by one point (x_1, y_1, z_1) on its surface and by its normal:

$$z = \frac{n_x}{n_z}(x_1 - x) + \frac{n_y}{n_z}(y_1 - y) + z_1$$ (B2)

The partial derivatives can be determined as follows:

$$\frac{\partial z}{\partial x} = -\frac{n_x}{n_z}$$ (B3)

$$\frac{\partial z}{\partial y} = -\frac{n_y}{n_z}$$ (B4)

Therefore, the square-root term simplifies to

$$\sqrt{\left(\frac{\partial z}{\partial x}\right)^2 + \left(\frac{\partial z}{\partial y}\right)^2 + 1} = \sqrt{\left(-\frac{n_x}{n_z}\right)^2 + \left(-\frac{n_y}{n_z}\right)^2 + 1}$$
$$= \sqrt{\frac{n_x^2}{n_z^2} + \frac{n_y^2}{n_z^2} + \frac{n_z^2}{n_z^2}}$$
$$= \left|\frac{1}{n_z}\right|$$ (B5)

The surface integral in Eq. (B1) simplifies to

$$\iint_A f(x, y, z) \, dA$$
$$= \iint_D \left|\frac{1}{n_z}\right| f\left(x, y, \frac{n_x}{n_z}(x_1 - x) + \frac{n_y}{n_z}(y_1 - y) + z_1\right) dy \, dx$$ (B6)

Now, we parameterize using v from 0 to $1 - u$ and u from 0 to 1, with

$$x(u, v) = x_1 + u(x_2 - x_1) + v(x_3 - x_1)$$ (B7)

$$y(u, v) = y_1 + u(y_2 - y_1) + v(y_3 - y_1)$$ (B8)

$$z(u, v) = \frac{n_x}{n_z}(u(x_1 - x_2) + v(x_1 - x_3)) + \frac{n_y}{n_z}(u(y_1 - y_2)$$
$$+ v(y_1 - y_3)) + z_1$$
$$= \frac{u}{n_z}((x_1 - x_2)n_x + (y_1 - y_2)n_y) + \frac{v}{n_z}((x_1 - x_3)n_x$$
$$+ (y_1 - y_3)n_y) + z_1$$ (B9)

Equation (B6) becomes

$$\iint_A f(x, y, z) \, dA$$
$$= \int_0^1 \int_0^{1-u} \left|\frac{1}{n_z}\right| f(x(u, v), y(u, v), z(u, v))|\boldsymbol{J}(u, v)| \, dv \, du$$ (B10)

where $\boldsymbol{J}$ is the Jacobian of the change of variables. The absolute value of its determinant is computed with

$$|\boldsymbol{J}(u, v)| = |(x_2 - x_1)(y_3 - y_1) - (x_3 - x_1)(y_2 - y_1)|$$ (B11)

Because both absolute value terms are not dependent on u and v,

$$\iint_A f(x, y, z) \, dA$$
$$= \left|\frac{\boldsymbol{J}(u, v)}{n_z}\right| \int_0^1 \int_0^{1-u} f(x(u, v), y(u, v), z(u, v)) \, dv \, du$$ (B12)

Applying the solution method from Eq. (B12) to the first integral in Eq. (19), with $\boldsymbol{\omega}_{\rm rel} = [\omega_1 \ \omega_2 \ \omega_3]^T$, $\boldsymbol{v}_{\rm rel} = [V_1 \ V_2 \ V_3]^T$, and $\boldsymbol{r}_p = [x \ y \ z]^T$,

$$f(x,y,z) = (\boldsymbol{n}^T(\boldsymbol{r}_p^\times \boldsymbol{\omega}_{\text{rel}}))(\boldsymbol{r}_p^\times \boldsymbol{v}_{\text{rel}})$$

$$= (n_x(y\omega_3 - z\omega_2) + n_y(z\omega_1 - x\omega_3) + n_z(x\omega_2 - y\omega_1))$$

$$\times \begin{bmatrix} yV_3 - zV_2 \\ zV_1 - xV_3 \\ xV_2 - yV_1 \end{bmatrix} \tag{B13}$$

Substituting $x(u,v)$, $y(u,v)$, and $z(u,v)$ for $n_z \neq 0$ from Eqs. (B7–B9),

$$f(u,v) = \beta \begin{bmatrix} (y_1 + u(y_2 - y_1) + v(y_3 - y_1))V_3 - \left(\frac{u}{n_z}((x_1-x_2)n_x + (y_1-y_2)n_y) + \frac{v}{n_z}((x_1-x_3)n_x + (y_1-y_3)n_y) + z_1\right)V_2 \\ \left(\frac{u}{n_z}((x_1-x_2)n_x + (y_1-y_2)n_y) + \frac{v}{n_z}((x_1-x_3)n_x + (y_1-y_3)n_y) + z_1\right)V_1 - (x_1 + u(x_2-x_1) + v(x_3-x_1))V_3 \\ (x_1 + u(x_2-x_1) + v(x_3-x_1))V_2 - (y_1 + u(y_2-y_1) + v(y_3-y_1))V_1 \end{bmatrix} \tag{B14}$$

where

$$\beta = n_x\left[(y_1 + u(y_2-y_1) + v(y_3-y_1))\omega_3 - \left(\frac{u}{n_z}((x_1-x_2)n_x \right.\right.$$
$$\left.\left. + (y_1-y_2)n_y) + \frac{v}{n_z}((x_1-x_3)n_x + (y_1-y_3)n_y) + z_1\right)\omega_2\right]$$
$$+ n_y\left[\left(\frac{u}{n_z}((x_1-x_2)n_x + (y_1-y_2)n_y) + \frac{v}{n_z}((x_1-x_3)n_x\right.\right.$$
$$\left.\left. + (y_1-y_3)n_y) + z_1\right)\omega_1 - (x_1 + u(x_2-x_1) + v(x_3-x_1))\omega_3\right]$$
$$+ n_z\left[(x_1 + u(x_2-x_1) + v(x_3-x_1))\omega_2 - (y_1 + u(y_2-y_1)\right.$$
$$\left. + v(y_3-y_1))\omega_1\right] \tag{B15}$$

We now apply the solution method to the second integral in Eq. (19):

$$f(x,y,z) = v_{\text{rel}}\cos\alpha\, \boldsymbol{r}_p^\times \boldsymbol{r}_p^\times \boldsymbol{\omega}_{\text{rel}}$$

$$= v_{\text{rel}}\cos\alpha \begin{bmatrix} -(z^2+y^2)\omega_1 + xy\omega_2 + xz\omega_3 \\ xy\omega_1 - (z^2+x^2)\omega_2 + zy\omega_3 \\ xz\omega_1 + zy\omega_2 - (x^2+y^2)\omega_3 \end{bmatrix} \tag{B16}$$

Substituting in $x(u,v)$, $y(u,v)$, and $z(u,v)$ for $n_z \neq 0$, the three terms of the vector $\boldsymbol{v}$, where

$$\boldsymbol{v} = \begin{bmatrix} v_1 \\ v_2 \\ v_3 \end{bmatrix} = \begin{bmatrix} -(z^2+y^2)\omega_1 + xy\omega_2 + xz\omega_3 \\ xy\omega_1 - (z^2+x^2)\omega_2 + zy\omega_3 \\ xz\omega_1 + zy\omega_2 - (x^2+y^2)\omega_3 \end{bmatrix} \tag{B17}$$

become

$$v_1 = -\left(\left(\frac{u}{n_z}((x_1-x_2)n_x + (y_1-y_2)n_y) + \frac{v}{n_z}((x_1-x_3)n_x\right.\right.$$
$$\left.\left. + (y_1-y_3)n_y) + z_1\right)^2 + (y_1 + u(y_2-y_1) + v(y_3-y_1))^2\right)\omega_1$$
$$+ (x_1 + u(x_2-x_1) + v(x_3-x_1))(y_1 + u(y_2-y_1) + v(y_3-y_1))\omega_2$$
$$+ (x_1 + u(x_2-x_1) + v(x_3-x_1))\left(\frac{u}{n_z}((x_1-x_2)n_x + (y_1-y_2)n_y)\right.$$
$$\left. + \frac{v}{n_z}((x_1-x_3)n_x + (y_1-y_3)n_y) + z_1\right)\omega_3 \tag{B18}$$

$$v_2 = (x_1 + u(x_2-x_1) + v(x_3-x_1))(y_1 + u(y_2-y_1) + v(y_3-y_1))\omega_1$$
$$- \left(\left(\frac{u}{n_z}((x_1-x_2)n_x + (y_1-y_2)n_y) + \frac{v}{n_z}((x_1-x_3)n_x\right.\right.$$
$$\left.\left. + (y_1-y_3)n_y) + z_1\right)^2 + (x_1 + u(x_2-x_1) + v(x_3-x_1))^2\right)\omega_2$$
$$+ \left(\frac{u}{n_z}((x_1-x_2)n_x + (y_1-y_2)n_y) + \frac{v}{n_z}((x_1-x_3)n_x\right.$$
$$\left. + (y_1-y_3)n_y) + z_1\right)(y_1 + u(y_2-y_1) + v(y_3-y_1))\omega_3 \tag{B19}$$

$$v_3 = (x_1 + u(x_2-x_1) + v(x_3-x_1))\left(\frac{u}{n_z}((x_1-x_2)n_x\right.$$
$$\left. + (y_1-y_2)n_y) + \frac{v}{n_z}((x_1-x_3)n_x + (y_1-y_3)n_y) + z_1\right)\omega_1$$
$$+ \left(\frac{u}{n_z}((x_1-x_2)n_x + (y_1-y_2)n_y) + \frac{v}{n_z}((x_1-x_3)n_x\right.$$
$$\left. + (y_1-y_3)n_y) + z_1\right)(y_1 + u(y_2-y_1) + v(y_3-y_1))\omega_2$$
$$- ((x_1 + u(x_2-x_1) + v(x_3-x_1))^2 + (y_1 + u(y_2-y_1)$$
$$+ v(y_3-y_1))^2)\omega_3 \tag{B20}$$

The double integral over u and v is now trivial and can be solved analytically. However, these equations are only valid for $n_z \neq 0$. If $n_z = 0$, then a similar approach can be done to obtain the following solutions for when $n_y \neq 0$ or $n_x \neq 0$, respectively.

Acknowledgments

The operation of this supercomputer is funded by the Canada Foundation for Innovation, Ministère de l'Économie, de la Science et de l'Innovation du Québec, and the Fonds de Recherche du Québec–Nature et Technologies.

References

[1] Shan, M., Guo, J., and Gill, E., "Review and Comparison of Active Debris Capturing and Removal Methods," *Progress in Aerospace Sciences*, Vol. 80, Jan. 2016, pp. 18–32.
     doi:10.1016/j.paerosci.2015.11.001

[2] Biesbroek, R., Innocenti, L., Wolahan, A., and Serrano, S. M., "e. Deorbit–ESA's Active Debris Removal Mission," *Proceedings of the 7th European Conference on Space Debris*, ESA Space Debris Office, Darmstadt, Germany, April 2017.

[3] Shrivastava, S. K., and Modi, V. J., "Satellite Attitude Dynamics and Control in the Presence of Environmental Torques—A Brief Survey," *Journal of Guidance, Control, and Dynamics*, Vol. 6, No. 6, 1983, pp. 461–471.
     doi:10.2514/3.8526

[4] Kucharski, D., Kirchner, G., Koidl, F., Fan, C., Carman, R., Moore, C., Dmytrotsa, A., Ploner, M., Bianco, G., and Medvedskij, M., et al., "Attitude and Spin Period of Space Debris Envisat Measured by Satellite Laser Ranging," *IEEE Transactions on Geoscience and Remote Sensing*, Vol. 52, No. 12, 2014, pp. 7651–7657.
     doi:10.1109/TGRS.2014.2316138

[5] Koshkin, N., Korobeynikova, E., Shakun, L., Strakhova, S., and Tang, Z. H., "Remote Sensing of the EnviSat and Cbers-2B Satellites Rotation Around the Centre of Mass by Photometry," *Advances in Space Research*, Vol. 58, No. 3, 2016, pp. 358–371.
     doi:10.1016/j.asr.2016.04.024

[6] Sommer, S., Rosebrock, J., Cerutti-Maori, D., and Leushacke, L., "Temporal Analysis of Envisat's Rotational Motion," *Proceedings of the 7th European Conference on Space Debris*, ESA Space Debris Office, Darmstadt, Germany, April 2017.

[7] Gómez, N. O., and Walker, S. J. I., "Earth's Gravity Gradient and Eddy Currents Effects on the Rotational Dynamics of Space Debris Objects: Envisat Case Study," *Advances in Space Research*, Vol. 56, No. 3, Aug. 2015, pp. 494–508.
     doi:10.1016/j.asr.2014.12.031

[8] Kanzler, R., Silha, J., Schildknecht, T., Fritsche, B., Lips, T., and Krag, H., "Space Debris Attitude Simulation–*i* OTA (In-Orbit Tumbling Analysis)," *Proceedings of the 2015 Advanced Maui Optical and Space Surveillance Technologies Conference*, Maui Economic Development Board, Inc., Hawaii, HI, Sept. 2015.

[9] Vallado, D., *Fundamentals of Astrodynamics and Applications*, 4th ed., Microcosm, Hawthorne, CA, 2013, Chap. 5, pp. 525, 551, 545, 574, 587.

[10] Vallado, D. A., Crawford, P., Hujsak, R., and Kelso, T. S., "Revisiting Spacetrack Report #3," *AIAA/AAS Astrodynamics Specialist Conference and Exhibit*, AIAA Paper 2006-6753, Aug. 2006.

[11] Hughes, P. C., *Spacecraft Attitude Dynamics*, Dover, Mineola, NY, 2006, pp. 59, 252, 263.

[12] Dormand, J. R., and Prince, P. J., "A Family of Embedded Runge–Kutta Formulae," *Journal of Computational and Applied Mathematics*, Vol. 6, No. 1, 1980, pp. 19–26.
     doi:10.1016/0771-050X(80)90013-3

[13] Pavlis, N. K., Holmes, S. A., Kenyon, S. C., and Factor, J. K., "The Development and Evaluation of the Earth Gravitational Model 2008 (EGM2008)," *Journal of Geophysical Research*, Vol. 117, No. B4, April 2012, Paper B04406.
     doi:10.1029/2011JB008916

[14] Gottlieb, R. G., "Fast Gravity, Gravity Partials, Normalized Gravity, Gravity Gradient Torque and Magnetic Field: Derivation, Code and Data," NASA CR 188243, 1993.

[15] Bruinsma, S. L., "The DTM-2013 Thermosphere Model," *Journal of Space Weather and Space Climate*, Vol. 5, Feb. 2015, p. A1.
     doi:10.1051/swsc/2015001

[16] Drob, D. P., Emmert, J. T., Meriwether, J. W., Makela, J. J., Doornbos, E., Conde, M., Hernandez, G., Noto, J., Zawdie, K. A., and McDonald, S. E., et al., "An Update to the Horizontal Wind Model (HWM): The Quiet Time Thermosphere," *Earth and Space Science*, Vol. 2, No. 7, 2015, pp. 301–319.
     doi:10.1002/2014EA000089

[17] Gómez, N. O., and Walker, S. J. I., "Eddy Currents Applied to De-Tumbling of Space Debris: Analysis and Validation of Approximate Proposed Methods," *Acta Astronautica*, Vol. 114, Sept.–Oct. 2015,

pp. 34–53.
     doi:10.1016/j.actaastro.2015.04.012

[18] Thébault, E., Finlay, C. C., Beggan, C. D., Alken, P., Aubert, J., Barrois, O., Bertrand, F., Bondar, T., Boness, A., and Brocco, L., et al., "International Geomagnetic Reference Field: The 12th Generation," *Earth, Planets and Space*, Vol. 67, No. 1, 2015, p. 79.
     doi:10.1186/s40623-015-0228-9

[19] Montenbruck, O., and Gill, E., *Satellite Orbits: Models, Methods, Applications*, Springer–Verlag, Berlin, 2012, p. 83.

[20] Kane, T. R., and Barba, P. M., "Effects of Energy Dissipation on a Spinning Satellite," *AIAA Journal*, Vol. 4, No. 8, 1966, pp. 1391–1394.
     doi:10.2514/3.3683

[21] Flegel, S., Gelhaus, J., Mockel, M., Wiedemann, C., and Kempf, D., "Maintenance of the ESA MASTER Model–Final Report," Inst. of Aerospace Systems TR 21705/08/D/HK, Braunschweig, Germany, 2011.

[22] Sagnières, L. B. M., and Sharf, I., "Stochastic Modeling of Hypervelocity Impacts in Attitude Propagation of Space Debris," *Advances in Space Research*, Vol. 59, No. 4, 2017, pp. 1128–1143.
     doi:10.1016/j.asr.2016.11.030

[23] Sagnières, L. B. M., and Sharf, I., "Evolution of Spacecraft Orbital Motion due to Hypervelocity Impacts with Debris and Meteoroids," *Proceedings of the 7th European Conference on Space Debris*, ESA Space Debris Office, Darmstadt, Germany, April 2017.

[24] Lips, T., Kanzler, R., Breslau, A., Karrang, P., Silha, J., Schildknecht, T., Kucharski, D., Kirchner, G., Rosebrock, J., and Cerutti-Maori, D., et al., "Debris Attitude Motion Measurements and Modeling–Observation vs. Simulation," *Proceedings of the 2017 Advanced Maui Optical and Space surveillance Technologies Conference*, Maui Economic Development Board, Inc., Hawaii, HI, Sept. 2017.

[25] Bastida Virgili, B., Lemmens, S., and Krag, H., "Investigation on Envisat Attitude Motion," *e.Deorbit Workshop*, European Space Research and Technology Centre, Noordwijk, The Netherlands, May 2014.

[26] Lemmens, S., Krag, H., Rosebrock, J., and Carnelli, I., "Radar Mappings for Attitude Analysis of Objects in Orbit," *Proceedings of the 6th European Conference on Space Debris*, ESA Space Debris Office, Darmstadt, Germany, April 2013.

[27] Chulliat, A., Macmillan, S., Alken, P., Beggan, C., Nair, M., Hamilton, B., Woods, A., Ridley, V., Maus, S., and Thomson, A., "The US/UK World Magnetic Model for 2015–2020: Technical Report," National Geophysical Data Center, NOAA, 2015.
     doi:10.7289/V5TB14V7

[28] Kucharski, D., Kirchner, G., Bennett, J. C., Lachut, M., Sośnica, K., Koshkin, N., Shakun, L., Koidl, F., Steindorfer, M., and Wang, P., et al., "Photon Pressure Force on Space Debris TOPEX/Poseidon Measured by Satellite Laser Ranging," *Earth and Space Science*, Vol. 4, No. 10, 2017, pp. 661–668.
     doi:10.1002/ess2.v4.10

[29] Cerri, L., Couhert, A., and Ferrage, P., "DORIS Satellites Models Implemented in POE Processing," International DORIS Service Rept. SALP-NT-BORD-OP-16137-CN, France, 2018, https://ids-doris.org/analysis-documents.html [retrieved 15 Jan. 2018].

[30] Pittet, J.-N., Silha, J., and Schildknecht, T., "Spin Motion Determination of the Envisat Satellite Through Laser Ranging Measurements from a Single Pass Measured by a Single Station," *Advances in Space Research*, Vol. 61, No. 4, 2018, pp. 1121–1131.
     doi:10.1016/j.asr.2017.11.035

[31] Silha, J., Pittet, J.-N., Hamara, M., and Schildknecht, T., "Apparent Rotation Properties of Space Debris Extracted from Photometric Measurements," *Advances in Space Research*, Vol. 61, No. 3, 2018, pp. 844–861.
     doi:10.1016/j.asr.2017.10.048

[32] Shakun, L., Koshkin, N., Korobeynikova, E., Melikiants, S., and Strakhova, S., "Monitoring of the Inoperative Envisat Satellite's Behaviour," *Odessa Astronomical Publications*, Vol. 26, No. 2, 2013, pp. 282–284.

[33] Lin, H.-Y., and Zhao, C.-Y., "An Estimation of Envisat's Rotational State Accounting for the Precession of its Rotational Axis Caused by Gravity-Gradient Torque," *Advances in Space Research*, Vol. 61, No. 1, 2018, pp. 182–188.
     doi:10.1016/j.asr.2017.10.014

[34] Silha, J., Schildknecht, T., Pittet, J. N., Kirchner, G., Steindorfer, M., Kucharski, D., Cerutti-Maori, D., Rosebrock, J., Sommer, S., and Leushacke, L., et al., "Debris Attitude Motion Measurements and Modelling by Combining Different Observation Techniques," *Proceedings of the 7th European Conference on Space Debris*, ESA Space Debris Office, Darmstadt, Germany, April 2017.